Synthesize battery degradation modes via a diagnostic and prognostic model

Matthieu Dubarry, Cyril Truchot, Bor Yann Liaw*

Hawaii Natural Energy Institute, SOEST, University of Hawaii at Manoa, 1680 East-West Road, POST 109, Honolulu, HI 96822, USA

HIGHLIGHTS

► A unique and novel inference technique for battery diagnosis and prognosis.
► A mechanistic model creates "what if" scenarios from degradation modes or their combinations.
► A physicochemical model based on electrode degradation mode, cell design and operating condition.
► Versatile for various chemistries, designs, sizes, geometries, operating or aging conditions.

ARTICLE INFO

ABSTRACT

Batteries are being used in increasingly complicated configurations with very demanding duty schedules. Such usage makes the use of batteries in multi-cell configurations to meet voltage, power, and energy demands in a very stressful manner. Thus, effective management and control of a battery system to allow efficient, reliable, and safe operation becomes vital, and diagnostic and prognostic tools are essential. Yet, developing these tools in practical applications is new to the industry, difficult and challenging. Here we present a novel mechanistic model that can enable battery diagnosis and prognosis. The model can simulate various "what-if" scenarios of battery degradation modes via a synthetic approach based on specific electrode behavior with proper adjustment of the loading ratio and the extent of degradation in and between the two electrodes. This approach is very different from the conventional empirical ones that correlate the cell parameters (such as impedance increases) with degradation in capacity or power fade to predict performance and life. This approach, with mechanistic understanding of battery degradation processes and failure mechanisms, offers unique high-fidelity simulation to address path dependence of the battery degradation.

© 2012 Elsevier B.V. All rights reserved.

1. Introduction

Battery performance and its degradation have significant consequence on reliability and safety of a battery system's function, which shall determine its feasibility and acceptance in the electric drive vehicle and electrical energy storage applications. To understand battery degradation mechanisms in a clear cause-and-consequence context remains very challenging today, and such a long struggle in the research community is likely due to the lack of simple and effective diagnostic tools to characterize degradation in situ through aging. Many postmortem analyses might reveal the cause of degradation and failure of a battery, but they are not useful in providing temporal resolution for practical battery monitoring, protection, and diagnosis during operation, nor can they provide useful information for prognosis. In our view, an effective battery diagnosis needs two major elements: a reliable method to determine the state of the battery with sufficient temporal resolution and a high-fidelity model to predict the performance under a duty regime. To achieve such a goal, here we present a unique mechanistic model that can reveal specific battery chemistry and its degradation modes. A degradation mode includes a degradation mechanism and consequences on battery performance, such as degrees in the fade of capacity, rate capability, and peak power; and cell properties, such as the increase in polarization resistance; with sufficient temporal resolution to tell the differences under various operating conditions.

The most effective and simple method of monitoring battery behavior is through the measurements of battery voltage, current, and temperature. In recent years, we, among others, noticed that the voltage and capacity responses of a Li-ion cell in a duty regime could be analyzed to derive information that can be used to estimate the state of a battery and its degradation [1–12]. Yet, most studies still focus only on capacity loss against cycle aging. Cell voltage not only depicts what electrochemical reactions are

occurring in the cell, its variations also reflect how the reactions progress in a duty regime. The ability to analyzing such cell voltage responses in different duty regimes is the key to understand cell behavior and degradation. To do so, a unique capability that we advocated recently is the analysis of incremental capacity (IC) [1–6], i.e. $dQ/dV = f(V)$, in diagnosis on a variety of commercial Li-ion batteries, including those made of $Li_xNi_{0.8}Co_{0.15}Al_{0.05}O_2$ (NCA), Li_xFePO_4 (LFP), $Li_xNi_{1/3}Mn_{1/3}Co_{1/3}O_2$ and $Li_xMn_2O_4$ composite (NMC + LMO), as reported in our previous work [1–6]. Others, like Honkura et al. [7,8] and Bloom et al. [9–12], prefer the analysis of differential voltage (DV), i.e. $dV/dQ = f(Q)$, and find it useful as well. Although both methods should yield similar information (in a reciprocal fashion), there is a distinct difference between the two: the IC refers to the cell voltage, which could be a direct and primary indicator of the battery state; whereas the DV refers to the cell capacity, which is an accumulative and secondary indicator that could vary with aging and degradation and lose its reliability as a reference in the course of aging.

Disregarding the differences in the two techniques, we also note that the interpretations of dQ/dV or dV/dQ obtained from the cell characterizations are not trivial at all to reveal cell behavior and its degradation modes. Particularly, since both electrodes in the cell contribute to the features (peaks and their shape) in the IC and DV curves, it is difficult to separate the electrode behavior and its contribution to the cell degradation. A technique that can resolve this issue would be highly desirable for battery monitoring, control and management. In our earlier work we solved this issue by using an analytic approach with qualitative results [5]. In this work, we developed a synthetic, mechanistic model using half-cell data obtained from experiments or literature to simulate the evolution of the IC and DV signatures, so we can quantify electrode contributions in cell degradation modes. This approach is applicable to most of the known chemistries used in the commercial cells and it can generate various "what if" scenarios for cell degradation modes as case studies to help us understand how cell degrades in a quantitative manner.

This approach conceptually follows the one described by Christensen and Newman in the early 2000s [13,14] and used by others such as Zhang et al. [15,16] and Delacourt et al. [17,18] to simulate cell degradation. A common theme in these approaches is the use of electrochemical models to simulate half-cell electrode behavior to compose the full cell charge and discharge curves. DV or IC curves could be derived in principle, yet results of such derivations have not been clearly reported in the literature to date. In contrast, some groups used experimental half-cell data and fitting techniques to compose dV/dQ curves [7,8,11,19–21] for some specific studies. These experimental approaches may provide the

benefits for case study and analysis; however, the applicability of the knowledge to other chemistries, cell designs, or operating conditions is limited, since they are after all empirical ones. Often, when substantial changes in cell chemistry, design, and operating conditions occur, the entire process has to be re-invested again to receive required fidelity and accuracy, which is quite costly and labor intensive.

The approach reported in this work combines both modeling and experimental techniques to provide a universal tool for diagnosis and prognosis. Our approach employs a modified equivalent circuit model (ECM) from which the cell performance is emulated from two separated half-cell modules each constructed from laboratory experimental data [22–26]. This approach offers the benefits of wide applicability of the model to various cell chemistries, designs, and operating modes; as well as the high fidelity as inhered from detailed extraction of the experimental data. In this work we use the Li_xFePO_4 (LFP) chemistry as a case study; but the approach is also validated with data obtained from our prior work on other chemistries [1–6].

2. Principles and model descriptions

The mechanistic model proposed in this work is composed of two layers: a top layer with cell configuration and inputs from cell operating and degradation modes and a sub-layer with half-cell modules that describe the electrode behavior. The modules use an ECM approach similar to that described in our previous work [22,23] to handle the electrode chemistry based on voltage and capacity variation as a function of rate. The top layer uses equations to assemble the two electrodes into a full cell configuration by considering electrode composition and loading ratio matching as a function of degree of degradation, degradation modes, and operating conditions.

The schematic of the mechanistic model and modeling approach is presented in Fig. 1. In contrast to conventional electrochemical or electrical models, in which the degradation results are outputs of the simulation, ours is a "backward looking" approach—the "what if" scenarios of degradation are the inputs to the simulation of the cell behavior in aging. The architecture of the model accommodates electrode-specific phenomena. It can also handle complicated cell and electrode configurations, including composite electrodes that comprise multi-composition mixtures of grains or core–shell micro-structured grains. The model is written in MATLAB® with architecture configured for effective functioning in computation, layer integration, and flexibility in conducting simulations of "what if" scenarios.
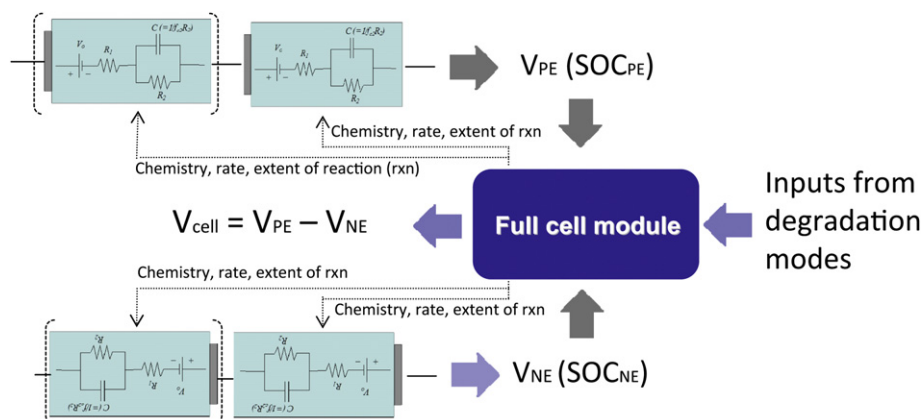

Fig. 1. Schematic of the modeling approach in this work.

2.1. Half-cell sub-layer modules

The half-cell module in the model is a key element in this work. For a typical single-composition-based electrode, the simulation is performed by feeding the ECM (Fig. 1) with parameters derived from half-cell data for each electrode [22,23]. For more complicated electrode architecture, the electrode ECM can be composed from several sub-ECMs each representing an active material composition in series (core–shell) or in parallel (mixture) configurations in the electrode. The electrode operation is considered in direct current, and the capacitance in the R//C circuit is ignored because the relaxation time corresponding to the R//C circuit is negligible compared to the duration of the test regimes discussed in this work. To derive resistance values, the open circuit potential (OCP) versus state-of-charge (SOC) or OCP = f(SOC) curve [1] needs to be established. This curve is established from the constant current charge and discharge regimes at a very low rate, such as C/25, in a half-cell. The electrode resistance value versus SOC correspondence is derived from pseudo Ohms' law approximation at any rate C and SOC as follows:

$$R_{exp}(C, SOC) = \frac{V_{OCP}(SOC) - V_C(C, SOC)}{abs(I_C)} \quad (1)$$

where R_{exp}(C,SOC) is the electrode resistance as a function of rate C and SOC as derived from the experimental data. V_{OCP}(SOC) and V_C(C,SOC) are electrode potential at open circuit and a given C rate, respectively. The abs(I_C) is the absolute value of the current at a given C rate. R_{exp}(C,SOC) is the sum of R_1 and R_2, where R_1 corresponds to the ohmic resistance calculated from the initial voltage drop after current is applied [23] and R_2 the faradic resistance that is rate and SOC dependent in the ECMs [22,23].

Hydro-Quebec and Timcal kindly provided the half-cell data for the LFP and graphite electrodes at different rates, respectively. For the LFP electrode, the parameters used to construct the sub-layer module are compiled from the discharge data at C/8, C/4, C/2, C/1, 2C and 4C. For the graphite electrode, the parameters are compiled from the charge data at C/50, C/5 and 5C. The electrode behavior at any other rates is simulated with interpolations or extrapolations.

Fig. 2 presents the simulation of the electrode behavior for (a) LFP discharge curves and (b) graphite charge curves at rates from C/25 to 2C with 0.1C intervals. For the convenience of discussion, the potential in the charge discharge curves simulated by the ECM will be denoted as $V_{electrode}$@C/n, where C/n is the imposed rate on the half cell. The model can simulate electrode behavior with high fidelity to extract capacity, resistance and kinetic information accurately for any rate within the range [23]. The fidelity can be assessed by a simple verification, as shown in Fig. 3. In this process, a specific rate (e.g. C/2 and 2C, respectively) is removed from the parameter matrix for the sub-layer module construction. The module thus constructed shall simulate the discharge curve for this rate and the result is compared with the experimental data. As shown in the figure, respectively, the simulation and experimental data for C/2 and 2C are in excellent agreement.

The separation of current density at the electrode and cell level is of great importance for this study in two accounts: (1) the current density applied to the cell should be treated differently in the electrodes, depending on the apparent area used by each electrode. (2) The current density at each electrode may also vary, depending on the aging condition and degradation mode. Although similar considerations might have been considered in the electrochemical models previously published by others [13–18], it has never been clear to us how such an aspect was incorporated in the models. We need to point out that in approaches with purely experimental fitting, it is quite resource demanding to consider this aspect
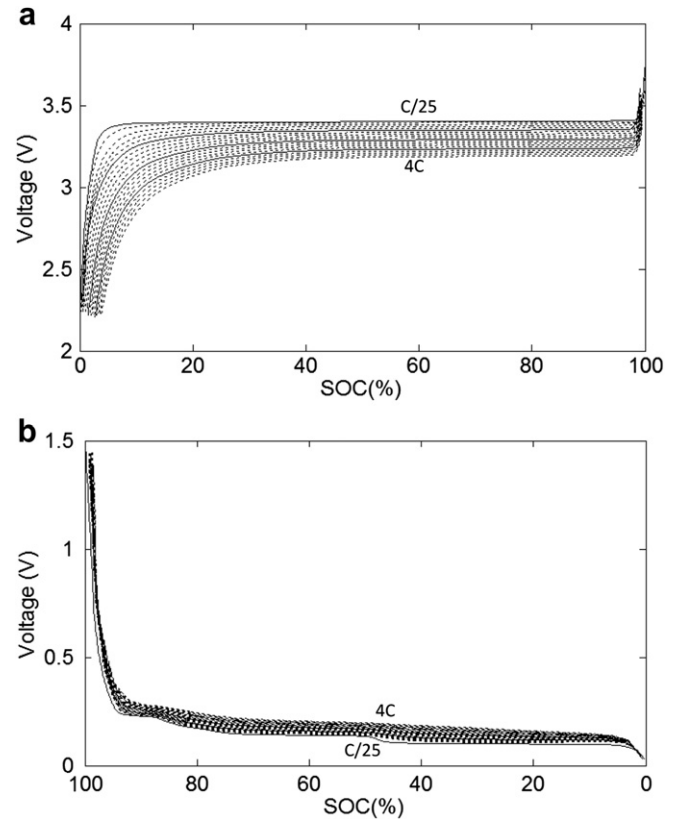

Fig. 2. (a) Simulation of the LFP electrode discharge regimes in a variety of rates from C/25 to 4C. (b) Simulation of the graphite electrode charge regimes from C/25 to 4C.

because half-cell data on a single electrode need to be tested over an extended range of conditions with sufficient details.

2.2. Full cell model

To emulate the cell behavior from the electrode sub-layers effectively, two parameters are essential: the loading ratio (LR) between the negative and the positive electrode (NE and PE); i.e. LR = Q_{NE}/Q_{PE}, and the initial irreversible capacity loss of the NE that compensates the SEI formation.

Fig. 4 presents an example using an hypothetical LFP cell, where an original LR, LR_o = 1.45, is chosen to emulate a typical high power (HP) cell design [27]. Because of the uncertainty in the initial
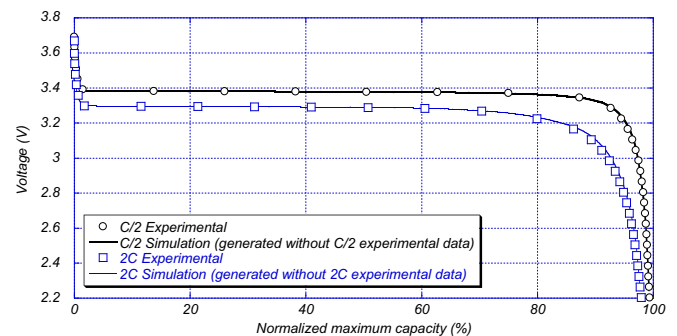

Fig. 3. Simulation of C/2 and 2C discharge curves of a Li || LFP cell. The data of each simulated rate (C/2 or 2C) was not used in the parameter matrix for the model construction and simulation, but as the basis for comparison with simulated results.
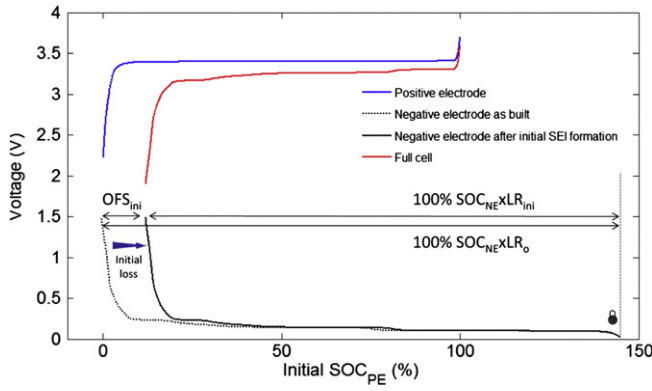
Fig. 4. Simulation of cell voltage as a function of SOC with the formation of the initial SEI layer.

Fig. 5. Simulation results for cell discharge regimes at C/25, C/5, C/2, C, 2C and 4C using a graphite ∥ LFP cell.

capacity loss at the NE, it is more convenient and reliable to use the SOC scale at the PE (SOC_{PE}) as the basis for the calculation of cell SOC. Thus, the $V_{NE} = f(SOC_{NE})$ curve can be transformed and scaled as a function of SOC_{PE}, $V_{NE} = f(SOC_{PE})$, as follows:

$$SOC_{NE} = (100\% - SOC_{NE})LR_o \qquad (2)$$

In this representation, 100% SOC_{NE} (fully delithiated NE) corresponds to 0% SOC_{PE}, whereas 0% SOC_{NE} (fully lithiated NE) should correspond to 145% SOC_{PE} because of the $LR_o = 1.45$ in the capacity conversion. All SOC values are presented in percentage.

It is well known that during the first cycle, the NE usually loses some capacity due to the formation of the SEI layer at the surface [28]. In Fig. 4, an irreversible 8.5% active material loss on the NE is assumed, which is equivalent to 12% capacity loss in the full cell, based on the LR calculation (i.e. 8.5% × 1.45 = 12%) and the fact that the full cell capacity is provided by the lithium content in the PE. For convenience in the simulation, an SOC_{PE} offset (OFS) and an apparent LR are used in the model to calculate the full cell behavior upon initial SEI layer formation. This initial offset (OFS_{ini}) corresponds to the shift of the V_{NE} in correspondence to the V_{PE} on the SOC_{PE} scale and the amount of graphite loss in the first cycle. The LR accounts for the graphite loss in the adjustment of the LR_o, i.e.:

$$LR_{ini} = \frac{100\% - OFS_{ini}}{100\%} LR_o \qquad (3)$$

In Fig. 4, an offset of $OFS_{ini} = 12\%$ SOC and $LR_{ini} = 1.3$ shall yield approximately the same composition after the initial irreversible capacity loss during cell formation (from 8.5% loss in NE and $LR_o = 1.45$).

Because of the SOC offset, Equation (2) needs to be modified as:

$$SOC_{NE} = (100\% - SOC_{NE})LR_{ini} + OFS_{ini} \qquad (2')$$

Equation (2′) is generally true, including situations with degradation as well.

Fig. 5 presents the simulated discharge curves of the full cell described in Fig. 2 at C/25, C/5, C/2, 1C, 2C, and 4C. The discharge curves, along with the rate capability (as expressed by Peukert curve) and the polarization resistance (both derived but not shown), are similar to those measured experimentally for cells in a commercial HP design tested in our laboratory [27]. The polarization resistance comprises both the ohmic resistance, including contact resistance and resistance derived from the conductance in the electron conductive network of the electrodes and the ionic conduction in the electrolyte; and the faradic resistance attributed
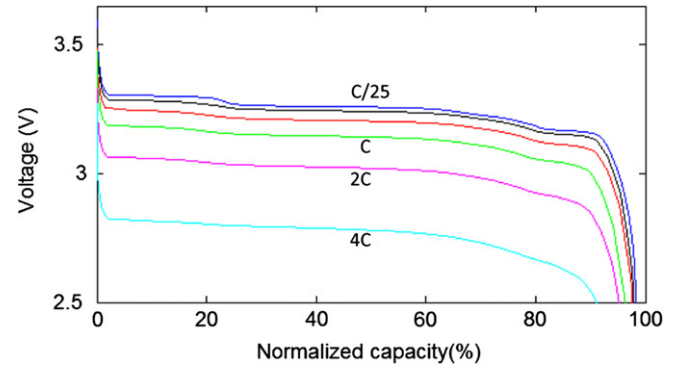
from charge transfer, mass transport in the porous electrode matrices and ion diffusion in the active materials.

The architecture and high fidelity of the model allows us to infer end-of-discharge/charge (EOD/EOC) SOCs and rest cell voltages (RCVs) for any given cut-off conditions. This is achieved by (1) calculating the pseudo-OCV of the cell (ps-OCV_{cell}) from the ps-$OCP_{PE\ or\ NE} = f(SOC_{PE})$ curve for each electrode, which is obtained from averaging the charge and discharge curves of each electrode measured at a very slow rate (such as C/25 or lower) [6]; (2) properly matching the SOC offset and LR; thus, the full cell ps-$OCV_{cell} = f(SOC_{PE})$ curve is constructed; and, (3) converting the SOC_{PE} to an SOC scale for the cell according to Equation (4):

$$SOC(V_{cell}) = \frac{SOC_{PE}(V_{cell}) - SOC_{PE}\left(OCV_{cell}^{EOD}\right)}{SOC_{PE}\left(OCV_{cell}^{EOC}\right) - SOC_{PE}\left(OCV_{cell}^{EOD}\right)} 100\% \qquad (4)$$

The EOD SOC depends on the given cutoff condition used; e.g. 2.5 V in this study. The RCV_{EOD} is inferred from the full cell ps-OCV_{cell} at the EOD SOC.

3. Simulation of cell degradation modes

Many possible cell degradation modes have been reported in the literature for various cell chemistries. It appears quite common in the literature that the loss of lithium inventory (LLI) due to the formation of SEI layers is often observed in the early stage of cell aging [4,6,14,16,17,20,29,30]. In addition, LLI can be induced by Li plating [31]. Another common degradation mode is the loss of active material (LAM) [4,6,14,16,17,20,29,30], which can be further categorized into four types, depending on the affected electrode and the degree of lithiation (i.e. predominantly in a lithiated or de-lithiated state) in which the LAM occurs. The origin of LAM could be due to isolation of the grains of the active materials from ionic or electronic conduction network in the electrode [32], dissolution of transition metal into the electrolyte solution, change in the electrode composition [33,34], or changes in the crystal structure of the active material (e.g. due to decomposition and oxygen evolution) that result in a reduction in the extent of lithiation [35]. Additional modes for capacity loss include the retardation in the charge-transfer kinetics at the electrode surface [6,30,34,36], ionic conduction in the active materials, or mass transport in the porous electrode matrices, which attributes to the increase in the faradic resistance; and increase of the ohmic resistance due to degradation in electrode contact or electrolyte conduction, as commonly observed in polarization resistance increase [13], and the formation of parasitic phases [35].

By properly adjusting parameters in both layers of the model, all these degradation modes can be simulated with sufficient flexibility to accommodate their variations. The full cell layer can handle the four types of LAM and LLI, whereas the half-cell sub-layer can handle ohmic resistance increase, faradic rate degradation, and formation of parasitic phases that are electroactive.

3.1. Loss of active material (LAM) and loss of lithium inventory (LLI)

Fig. 6 presents the simulation of the four types of LAM at C/25 up to 50% loss of capacity (with 10% increments, in dotted lines). The initial and the state of 50% capacity loss, respectively, are denoted by solid lines. Each type of LAM is noted by the electrode in which it occurs (in the subscript), with a prefix that specifies the state of lithiation; i.e. "li" for lithiated and "de" for delithiated.

A loss of active material (AM) will affect the LR. Disregarding if the AM is lithiated or not, as long as some PE AM is lost, the LR will increase. Similarly, the LR will decrease if NE AM is lost. Given a 50% AM loss, the LR will double if some PE AM is lost and reduce by half if some NE AM is lost. The evolution of the LR upon a given percentage of LAM can be expressed as:

$$LR = LR_{ini}\left(\frac{100\% - \%LAM_{deNE} - \%LAM_{liNE}}{100\% - \%LAM_{dePE} - \%LAM_{liPE}}\right) \quad (5)$$

The LAM will also change the rate on the affected electrode, since it decreases both the material content that can accept charge and the active surface area and thus increases the current density. Therefore, the electrode-specific rates C_{PE} and C_{NE} can be expressed as a function of the "imposed" rate (C_{imp}) on the cell, the extent of degradation (in percentage) in the electrode and, on the NE, the LR:

$$C_{PE} = \frac{100\%C_{imp}}{100\% - \%LAM_{dePE} - \%LAM_{liPE}} \quad (6)$$

$$C_{NE} = \frac{100\%C_{imp}}{LR(100\% - \%LAM_{deNE} - \%LAM_{liNE})} \quad (7)$$

The evolution of LR and the C_{PE} and C_{NE} are not affected by the state of lithiation in the LAM. The electrochemical behavior of the cell $V_{cell} = f(SOC_{PE})$ is however affected.

In the charge regime, were the PE suffering from LAM (LAM$_{liPE}$), less charge is released from the PE when it reaches EOC. Consequently, the NE should have a higher EOC SOC$_{NE}$ than that of the prior cycle. Vice versa, were LAM occurring in the NE (LAM$_{deNE}$), by the time the PE is fully delithiated, the NE will have a lower SOC$_{NE}$ than that of the prior cycle, since a less amount of NE will accept the same charge. Schematics of both scenarios are presented in Fig. 6(a) for the LAM$_{liPE}$ and Fig. 6(c) for the LAM$_{deNE}$, respectively. It has to be noted that when 0% SOC$_{NE}$ is reached earlier than 100% SOC$_{PE}$ on the PE scale (dotted line on Fig. 6(c)) the cell is at risk of Li plating (cf. Section 3.2.3) because the NE is fully lithiated before the PE completely releases all its Li ions. In the simulation, as the condition of EOD does not change, the OFS$_{ini}$ remains the same and a simple adjustment of the LR is sufficient to emulate both cases.

In the discharge regime, the LAM-affected electrode will complete its electrochemical reactions at a higher SOC. Contrary to the charge regime; the LAM does not affect the state of the affected electrode in the beginning of the discharge regime (i.e. EOC SOC). Fig. 6(b) and (d) shows the case for the LAM$_{dePE}$ and LAM$_{liNE}$, respectively. Additional adjustment to the model is needed to simulate these two cases, since the EOD of the affected electrode is evolving with aging; so is the LR matching with the opposite electrode. The simulation requires adjustments in both LR and SOC offset. By keeping the EOC on the SOC$_{PE}$ scale unchanged, we simulate these LAMs by adjusting the LR and SOC offset according to the percentage of LAM and the relative loading matching of the two electrodes as follows:

$$OFS = OFS_{ini} + LR \times \%LAM_{liNE} + \frac{LR}{LR_{ini}} \times \%LAM_{dePE} \quad (8)$$

The model can also simulate the scenarios involving LLI. LLI occurs when reversible Li ions are partially consumed by parasitic reactions in the cell. LLI commonly occurs during charging when Li ions are used to grow the passivation layer on the NE. It may also occur during discharging if a passivation layer consuming Li is growing on the PE. Fig. 7 illustrates the case for a charge regime, where LLI does not affect the EOC SOC$_{PE}$, since the PE is releasing the Li-ions. The SOC$_{PE}$ at EOC of the NE is however evolving with aging and becoming lower cycle by cycle; since less Li ions are inserting in the NE each time. This results in the evolution of the
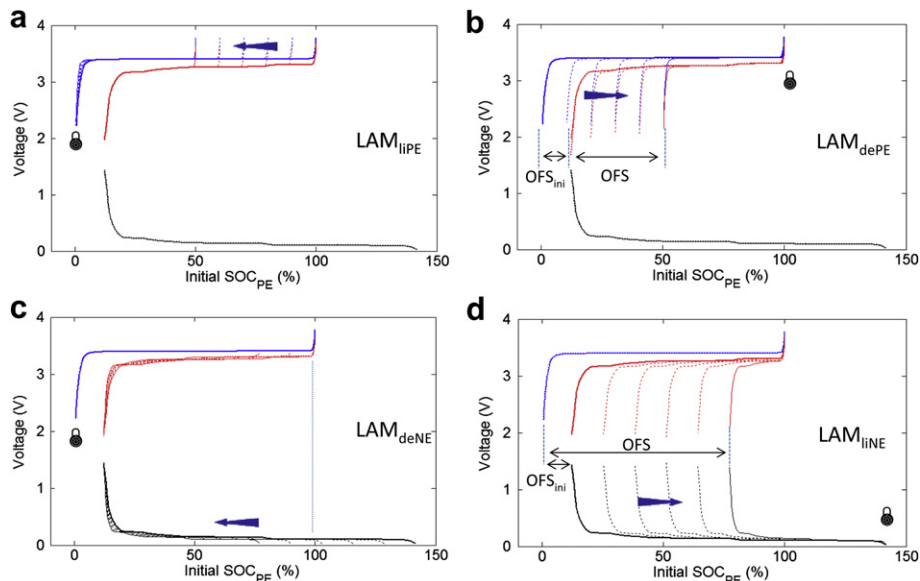

Fig. 6. Simulation of the four types of loss of active material (LAMs) at C/25 in delithiated PE (dePE), lithiated PE (liPE), delithiated NE (deNE) and lithiated NE (liNE).
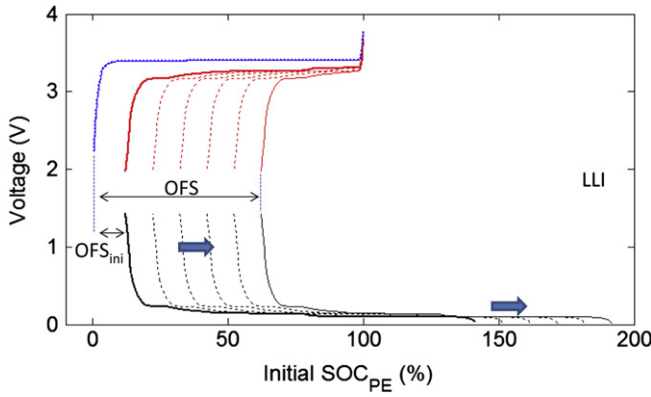
Fig. 7. Simulation of the LLI degradation mode at C/25.

loading correspondence in the discharge curves between the two electrodes, as shown in Fig. 7. The correspondence can be adjusted by including the percentage of LLI in the calculation of the SOC offset as follows:

$$OFS = OFS_{ini} + LR \times \%LAM_{liNE} + \frac{LR}{LR_{ini}} \times \%LAM_{dePE} + \%LLI_{ch} - \%LLI_{dis}$$

$$(8')$$

The subscripts of "ch" and "dis" are for "charge" and "discharge" regimes, respectively. In the follow-on discussion, only LLI$_{ch}$ is considered; thus, the notation LLI refers to LLI$_{ch}$, unless specified.

3.2. Ohmic resistance increase, faradic rate degradation, and formation of parasitic phase

3.2.1. Ohmic resistance increase (ORI)

Fig. 8(a) shows a simulation of a scenario of ohmic resistance increase (ORI) by 100% in the PE and 66% in the NE and their impacts on a 2C discharge curve of a cell. In this case, the potential of each electrode is altered by the amount of ORI with no change in the LR or the SOC offset. Since the half-cell ECM in the sub-layer computes the initial electrode potential response at a given rate C, a potential correction, due to the additional IR drop induced by the percentage of ORI (%ORI), needs to be introduced as follows:

$$V_{cell}@C_{imp} = V_{PE}@C_{PE} - C_{PE}R_{PE}\left(\frac{\%ORI_{PE}}{100\%}\right) - V_{NE}@C_{NE}$$
$$+ C_{NE}R_{NE}\left(\frac{\%ORI_{NE}}{100\%}\right) \quad (9)$$

where R_{PE} is the ohmic resistance associated with the PE and R_{NE} the one associated with the NE in the corresponding R_1 in the sub-layer module ECMs, respectively.

3.2.2. Faradic rate degradation (FRD)

Faradic rate degradation (FRD) occurs when an electrode does not react with Li ions at the same kinetic rate in aging. FRD induces changes in the electrochemical behavior of the cell, such as IC peak broadening, and increase in R_2 in the corresponding sub-layer module ECMs. Fig. 8(b) shows a simulation for FRD in a C/5 discharge of a LFP electrode due to aging. Because of FRD, the voltage plateau is shortened (i.e. as a result of the slower kinetics, so the disparity in the extent of reaction throughout the electrode increases with aging) and the voltage decrease toward the EOD
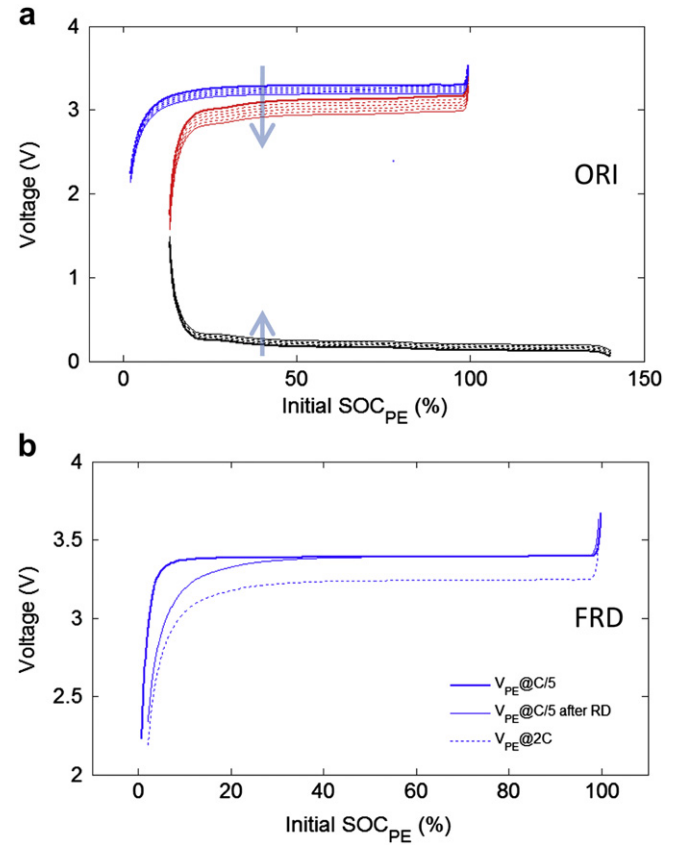

Fig. 8. Simulation of (a) ohmic resistance increase (ORI) at 2C and (b) faradic rate degradation (FRD).

becomes more gradual than before. Such consequences make the shape of the discharge curve resemble to that of a higher rate (at 2C in the example), although the initial ohmic IR drop remains the same. Thus, the FRD is simulated by "downgrading" the reaction kinetics to a lower rate (C_{RD}) than the initial one imposed on the PE (C_{PE}), while maintaining the initial IR drop to its C_{PE} value, and by introducing a rate degradation factor (RDF) defined as:

$$RDF_{PE} = \frac{C_{RD}}{C_{PE}} \quad (10)$$

in the rate calculation for each electrode as follows:

$$C_{PE} = \frac{100\%RDF_{PE}C_{imp}}{100\% - \%LAM_{dePE} - \%LAM_{liPE}} \quad (6')$$

$$C_{NE} = \frac{100\%RDF_{NE}C_{imp}}{LR_{ini}(100\% - \%LAM_{deNE} - \%LAM_{liNE})} \quad (7')$$

To hold the initial IR drop unchanged, Equation (9) is modified as follows:

$$V_{cell}@C_{imp} = V_{PE}@C_{PE} - C_{PE}R_{PE}\left(\frac{\%ORI_{PE}}{100\%} + RDF_{PE} - 1\right)$$
$$- V_{NE}@C_{NE} + C_{NE}R_{NE}\left(\frac{\%ORI_{NE}}{100\%} + RDF_{NE} - 1\right) \quad (9')$$

The same approach can be applied to the temperature effect on reaction kinetics. As the temperature of an electrode changes, the reaction kinetics often vary as well.

3.2.3. Formation of parasitic phase (FPP)

A parasitic phase can be either Li reactive or not. Either case can be simulated using this model. If a non-reactive parasitic phase is formed, the degradation mode can be modeled as a LAM on the affected electrode. The type of LAM (on lithiated or delithiated AM) is determined by the mass and charge balance between the AM and the parasitic phase composition.

If the parasitic phase is Li reactive, the affected electrode will resemble a "composite" electrode, showing the potential changes of all electrochemically active phases in the electrode reactions. The potential and the associated capacity variation in the electrode reaction are referred to as "signature" to facilitate following discussions. The signature of the main component in the electrode should diminish gradually through the course of degradation, while the signature of the parasitic phase continues to grow in a progressively apparent fashion. This evolution of signature can be emulated by adding sub-layers in the model; each representing the behavior of a component in the electrode in series or parallel with one another. The potential of the "composite" electrode is thus simulated in the degradation mode.

An example is provided in Fig. 9 for the LFP electrode. It has been reported in the literature that exposing LFP raw materials in the air could result in the formation of $Li_xFePO_4(OH)_x$ phases [37,38]. These phases and their electrochemical behavior have been characterized in Refs. [39–41]. The literature data of a LFP cell with AM aged in the air can be adopted in the model and the cell performance simulated. The data for the hydrated LFP phase in Fig. 9 are taken from Ref. [39] where the C/50 charge discharge data are available. Fig. 9 presents the evolution of cell voltage vs. SOC_{PE} curves in a graphite || LFP cell with 0% (thick solid line) 10%, 20% (dashed lines) and 30% (thin solid line) hydrated phase presence. The hydrated phase is electroactive at low potentials; thus, the shape of the PE potential curve at low SOCs is modified to reflect the nature of the electrochemical behavior of the PE composition changes. The hydrated phase can only take up to 0.8 Li per formula even at low rates [39]. Thus, if 30% of the hydrated phase is present, the EOD SOC should be offset by $(1–0.8)*30\% = 6\%$. The presence of 10% hydrated phase is not going to create any noticeable changes in capacity with the existing cutoff, because the induced SOC offset and changes in the OCV $= f(SOC)$ curve occur in the range of OFS_{ini}. However, if 30% of the hydrated phase is present, it will induce a noticeable cell signature change and a small capacity loss.

Similar phenomena could also happen in the NE; for instance, Li plating is a well-known phenomenon. Li plating often occurs under two conditions: (1) if the IR_{NE} drop of the NE during charging makes the NE potential goes ≤ 0 V or (2) if the LAM_{deNE} is significant to reach a condition where overcharging in NE happens

(dotted line in Fig. 6(c)). If the plated Li is passivated progressively [42], it will result in additional LLI. Therefore, increasing the $\%LLI_{ch}$ in Equation (8′) shall enable the simulation of this scenario.

3.3. Multiple processes in a degradation mode

In the previous sections, the simulation of individual degradation mode (e.g. LAM, LLI, ORI, FRD and FPP) was discussed. By combining all the equations, this model is capable of simulating degradation modes with multiple concurrent processes in an electrode or both. Fig. 10 presents some case studies. Fig. 10(a) shows a scenario of degradation mode comprising a logarithmic increase of LAM_{liNE}, an exponential increase of LAM_{dePE} and a linear progression of LLI over 100 cycles of aging. The model computes the evolution of the contributions to capacity fade from these three phenomena as a function of cycle number (Fig. 10(a)) and simulates the electrode potential and cell voltage vs. SOC changes from the initial to the condition at the end of 100-cycle aging (Fig. 10(b)) with proper LR and SOC offset adjustments.

This versatility to simulate complicated degradation modes at any rate and the capability of predicting capacity loss, EOD SOC,
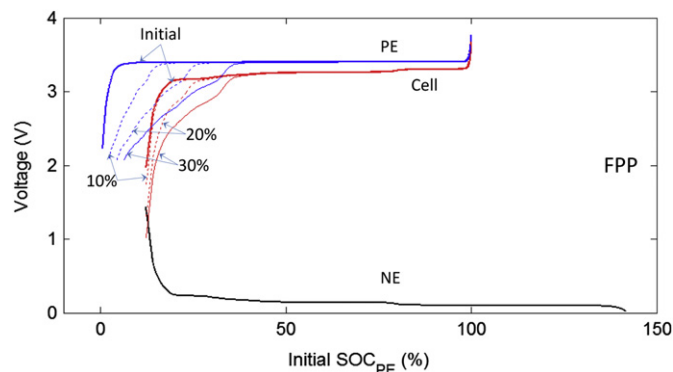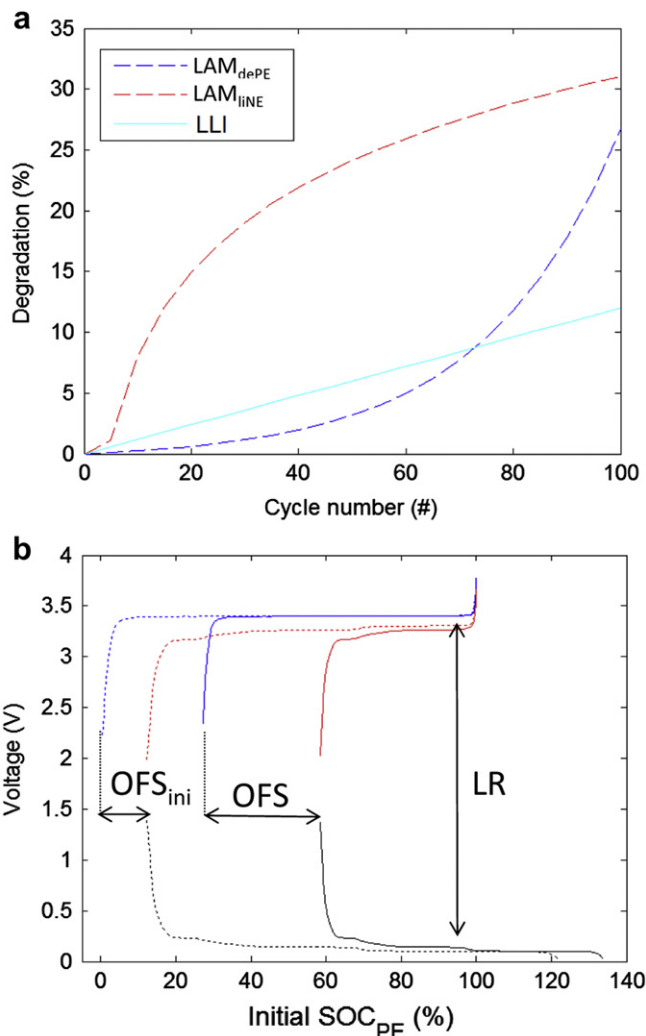
Fig. 9. Simulation of a graphite || LFP cell discharge curves with corresponding PE potential versus SOC_{PE} curves in the presence of 0% (thick solid line), 10%, 20% (both in dashed lines), and 30% (thin solid line) of hydrated phase, respectively.

Fig. 10. (a) Simulation of capacity loss versus cycle number in multiple concurrent degradation modes of LAM_{dePE}, LAM_{liNE}, and LLI, and (b) the corresponding electrode potential at PE and NE and cell voltage versus SOC_{PE} at the initial and final stage of degradation.

RCV$_{EOD}$, IC (dQ/dV) and DV (dV/dQ) signatures are presented below to show the applicability of this mechanistic modeling approach for battery diagnosis and prognosis.

4. Applications to battery diagnosis and prognosis

4.1. Capacity and EOD SOC changes

To exemplify the utility of this model for evaluation of commercial cells, two distinct cell designs of the same chemistry based on graphite NE and LFP PE were compared: a high power (HP) design with a high graphite content for high rate capability and a high energy (HE) design of a lower LR with low rate capability and high energy content (see details in Ref. [27]). The interest in this study is to study the effect of LLI on capacity retention and the corresponding change in the SOC range used in the course of aging. This analysis is motivated by our previous study [4] of an HE cell in which the cell exhibited a unique behavior in its first 100 cycles of aging where capacity fading was observed at lower rates but not higher ones, yet the cell seemed discharged to a lower SOC progressively. It is curious for us to figure how the LLI results in such a phenomenon and if we can apply the knowledge learned from this exercise to HP design.

Fig. 11(a) presents the capacity retentions and (b) EOD SOC evolution simulated for 50% LLI in three scenarios: the C/25 discharge curve for this chemistry and the 2C discharge curves for the HE and HP design, respectively. The simulation suggests that the trend of capacity fade for the HP cell @2C is similar to that of C/25; and, it is proportional to the amount of LLI. In the HE design, the trend of capacity fade is different from the other two. At first, the capacity @2C is much lower than the other two (because of the HE design) but stays stable over a range of cycles, although LLI is recurring in the cell. Upon reaching 15% LLI, the capacity fade begins to appear and follows the same trend as the other two. The simulation results are consistent with our experimental observations reported in Ref. [4]. Fig. 11(b) shows the evolution of the EOD SOC, which tends to increase slightly for C/25 and HP@2C

discharges but decreased by 20% for the HE@2C discharge before stabilizing and following the same trend with the other two.

The peculiar behavior of the HE design can be explained by plotting the evolution of the electrodes $V = f(SOC)$ in all three cases. Fig. 11(c) and (d) present the evolution of the potential of PE, NE and the cell voltage in the course of degradation for the HP and HE designs, respectively. The dotted lines represent the initial OCV $= f(SOC)$ curves for both electrodes. The solid lines are the initial discharge curve of the cell at 2C and the corresponding potential curves for the electrodes. The dashed lines are the discharge curves showing the capacity fade induced by consecutive LLI in 10% increments up to 50% of LLI.

In the HP design (Fig. 11(c)), the cell can deliver capacity close to its maximum at 2C and the capacity-limiting electrode is the NE. This is not the case for the HE design. Because of the lower inhered rate capability, the capacity is initially limited by the PE.

As described in Section 3.1, due to LLI the NE loading progressively shifts toward higher SOCs. Since the NE is the limiting electrode for the HP design, its capacity fade will be reflected immediately in the cell capacity loss; on the contrary in the HE design, as long as the PE is limiting the capacity, the NE capacity fade would not be detected. The capacity fade will appear only when the NE loading is shifted sufficiently to make the NE capacity limiting.

The evolution of the EOD SOCs in the aging process can be explained similarly. For the HP design, the cutoff condition at EOD is determined at the NE, and this scenario remains the same in the aging. Thus, the EOD SOC for the C/25 discharge is almost the same, although gradually sliding to higher values is predicted. The sliding of SOC toward high values for both C/25 and 2C discharges is imputable to the overall capacity loss and an unaltered rate capability. The unaltered rate capability suggests the same difference in capacity at the EOD between C/25 and 2C through aging. As the maximum capacity is decreasing in the course of aging, this constant capacity difference represents a progressively higher EOD SOC. For the HE design, the capacity difference between C/25 and 2C is not constant but decreasing through the course of aging.
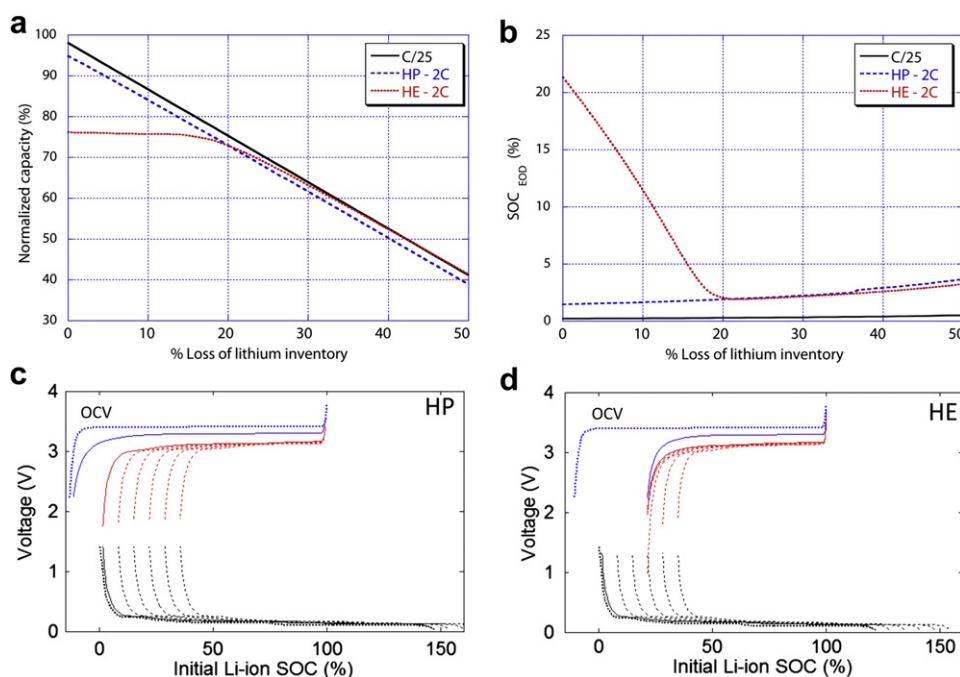

Fig. 11. (a) Capacity retention and (b) EOD SOC evolution as a function of %LLI and electrode potentials, cell voltage as a function of SOC simulated with a hypothetical 50% LLI for (c) HP and (d) HE designs.

Therefore, the EOD SOC at 2C decreases until the NE becomes the capacity-limiting electrode.

4.2. Cell diagnosis and prognosis

Since the model can produce results for inference of battery degradation modes, it is a powerful technique for battery diagnosis and prognosis. Here the derivation of two useful pieces of information, the incremental capacity (IC) and differential voltage (DV) curves, is illustrated to show the utility of this approach. Both IC and DV signatures have been used as inference techniques capable of revealing battery degradation mechanisms and quantifying the degree of degradation in a cell. The ability to derive these signatures is an advancement in the inference techniques, since degradation results can now be simulated under various scenarios to help us identify the mechanisms with much less uncertainty. For instance, in the comparison of the four types of LAMs, we can identify which mode might occur in the cell using dQ/dV or dV/dQ analysis, without any ambiguity. In some cases where some degradation modes may give similar results in the capacity loss, we can simulate each hypothesis in the model to see if subtle differences can be identified among various scenarios. Thus, in principle, through careful analysis, additional testing, and simulation, we should be able to test various hypotheses and identify the mechanism with more quantitative information; and, verify and enhance the inference technique.

A cell voltage comprises a proper matching of the $V_{NE} = f(SOC)$ and $V_{PE} = f(SOC)$ curves based on their loading ratio correspondence and degradation modes, as executed in the top layer module of the model. The evolution of the cell voltage in an aging process is thus attainable from the simulation. Fig. 12 presents the C/25 discharge curves with 30% capacity loss for the four LAM and LLI modes. These degradation modes not only show a variety of capacity loss scenarios, from almost none in 30% LAM$_{deNE}$ to about 50% in 30% LAM$_{liNE}$, but also produce a variety of $V_{cell} = f(SOC)$ signatures. These variations in cell performance characteristics are the basis for battery diagnosis and prognosis by inference.

Fig. 13 shows the variations in the IC signature for six degradation modes: i.e. 30% in four LAMs and LLI, and 100% ORI. In the figure, the heavy solid line represents the initial state, the thin solid line the final state, and the dotted lines 1/5th increments in the degree of degradation. Fig. 14 shows the same results for the DV analysis. To facilitate discussions, the same convention as in our previous work will be used [5,6]. The graphite staging phenomena are numbered as ❶ to ❺, where ❶ is the reaction from LiC$_{12}$ to LiC$_6$ and so on, and ❺ the last staging transition leading to the delithiated graphite (as shown in Fig. 12). In the $dQ/dV = f(V)$ curve, these five staging phenomena coupled with the LFP potential

plateau are observed as five IC peaks [4]. In the DV analysis, these five staging phenomena become valleys in the $dV/dQ = f(Q)$ curve. There are four $dV/dQ = f(Q)$ peaks representing non-stoichiometry in the single-phase regions (solid solution), as noted by A to D. The peak correspondence is labeled in the upper left plot (a) in each figure.

The utility of these IC and DV curves is further explained here. As shown in the left column of Figs. 13 and 14, LAM$_{liPE}$, LAM$_{deNE}$ and LLI show similar IC and DV signatures. They share a common theme that the graphite cannot be lithiated to the same level as it was initially; so, the main feature in the respective signatures is the loss of intensity in the first peak ❶ on the IC curve and the valley ❶ on the DV curve. For the LAM$_{liPE}$ and LLI, the intensity of peak/valley ❷ is affected only when ❶ is completely lost. In the LAM$_{deNE}$, all ❷ to ❺ peaks/valleys are fading from the beginning, thus LAM$_{deNE}$ can be unambiguously identified. It is interesting to note that it is almost impossible to distinguish between LAM$_{liPE}$ and LLI using the DV analysis in this case. It is however possible in the IC analysis, since peak ❺ is shifting toward higher voltages faster for LLI than for LAM$_{liPE}$, although it might be difficult to decipher between the two from the C/25 IC signature, especially for small capacity fade ($<5\%$) and if the PE potential is really a constant potential plateau.

There is a shift in the trend of signature evolution in LAM$_{dePE}$ when the PE becomes the capacity-limiting electrode. Before the shift, no changed are observed; beyond, the last graphite staging process cannot be completed anymore; thus, the peak ❺ in the IC curve and peak D in the DV curve are disappearing. This disappearance is followed by higher losses in peaks/valleys ❸ and ❹.

In the case of LAM$_{deNE}$, all the IC peaks are shrunk (since less graphite is involved in the reactions) except peak ❶ that increases. This is because LR > 1, and with LAM$_{deNE}$, more and more capacity in the staging ❶ plateau is accessible in the intercalation. In the DV representation, the accessible capacity in valley ❶ increases; thus, all the other valleys are shrinking, because the total capacity is constant. Hence, all DV peaks are moving toward lower capacities.

The lower right-hand plots in Figs. 13 and 14 are the results of ORI, which indicate a shift of all IC peaks toward lower voltages on the IC curves; in contrast, no change at all for DV peaks in the DV curves. This is due to the fact that the ORI only affects the cell voltage, not the capacity. Therefore, without capacity fade, the effect can only be seen on a voltage scale.

In summary, both IC and DV analyses offer merits and drawbacks for battery degradation inference. One should consider their merits to choose proper tools to highlight different aspects of the degradation phenomena. Although capacity quantification might be easier with the DV analysis, IC analysis may inhere a better sensitivity to decipher degradation modes. It reflects cell degradation signature on a voltage scale, which provides a better reference to the state of the battery than the capacity scale that varies with aging.

This study shows that, in the case of graphite ‖ LFP chemistry, the derivation of signature for various cell degradation modes is rather feasible, but it is difficult to distinguish between LAM$_{liPE}$ and LLI unambiguously. This is due to the fact that the LFP used in the example has a flat potential plateau and good rate capability. We trust that the two modes would be distinguishable in other chemistries, or if the LFP electrode is carefully characterized with better resolution in rate and temperature effects.

5. Implications to battery testing

In addition to the derivation of IC and DV signatures and their evolutions in aging, the model can allow us emulate other interesting features to aid the understanding of battery testing data
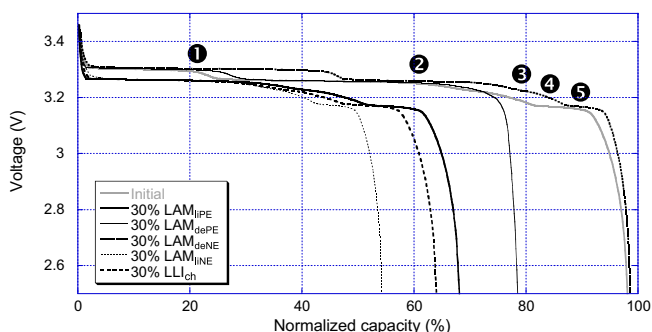

Fig. 12. $V = f(Q)$ for an HP cell at the initial state and with 30% of degradation from various modes comprising the four types of LAMs and LLI at C/25.
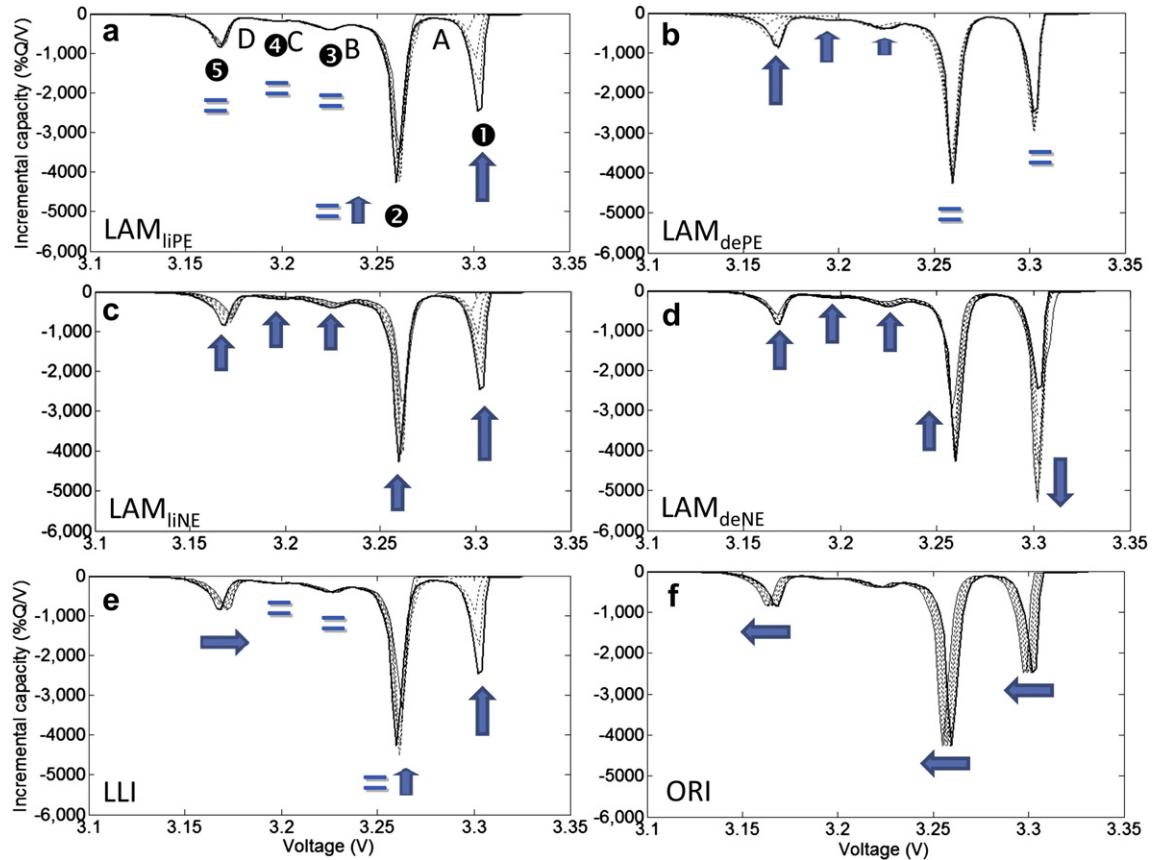
Fig. 13. IC signatures from the initial state (thick solid line) and at the end of 30% degradation (thin solid line) with 1/5th increment (dotted lines) for (a–d) each of the four LAMs, (e) LLI, and (f) a 100% ohmic resistance increase (ORI) at C/25.

usually received from typical cell evaluation procedures [1–6]. Following are some useful illustrations to explain such aspects:

5.1. OCV = f(SOC) evolution

Fig. 15(a) presents the evolution of ps-OCV = f(SOC) curves simulated for different LAMs and LLI, where Fig. 15(b) shows the evolution of the ps-OCV = f(SOC) curve with 30% LLI in 3% increments. The examples reveal that there are variations in the ps-OCV = f(SOC) curves, depending on the modes and the degree of degradation. As being revealed in the test data [6], degradation modes may change the correspondence between the PE and NE loading.

Understanding such cell voltage evolution in aging is important because one of the most effective way to determine the cell SOC is to measure the rest cell voltage (RCV) and use an OCV = f(SOC) curve to infer the SOC value [6,43]. If the correlation between the RCV and SOC varies with aging, the inference of SOC should gradually lose its accuracy. This issue thus introduces a very difficult hurdle to overcome in battery control and management. For instance, in Fig. 15(a), it is shown that for a RCV = 3 V, the SOC of the cell is 7% at the initial state but could be in the range of 2% and 7% after aging depending on degradation scenarios. This indicates that to accurately determine the SOC of the cell from the RCV, it is essential to calibrate the ps-OCV = f(SOC) as often as possible through reference performance tests (RPT) at low rates upon aging [6], which is quite impractical. Another example showing the issue with the evolving EOD SOC = f(RCV$_{EOD}$) is presented in Fig. 15(c), in which the RCV evolution is shown with

up to 30% LLI in a HE cell (following the case of Fig. 11(b)). Although the EOD SOC evolution seems straightforward with a steady decrease over aging, the RCV$_{EOD}$ evolution is affected not only by the voltage plateaus (see ❺ in Fig. 15(c)) where the OCV is constant over a range of SOCs but also by the evolution of the ps-OCV = f(SOC) curves. Indeed, the RCV of 2.9 V, which should correspond to 2.5% SOC initially, now is 5% SOC after aging. These evolutions of both RCVs and SOCs have been observed experimentally for commercial LFP cells [4].

Our model could be used as a calibration tool to calculate the ps-OCV = f(SOC) curves evolution at any stage of degradation, which can be validated between two RPTs, for diagnosis. It could also be used for prognostics by extrapolation from previous RPTs, if the degradation modes were identified from the test data and the results quantified to feed the model. Since our model does not require much computation, the results can be easily used to compose lookup tables (from single-electrode half-cell data); thus, our approach can be easily implemented into battery management systems (BMS) to improve SOC and SOH tracking.

5.2. Effect of the electrode-specific rate on the cell behavior

Another interesting capability derived from this study is the ability to assess the effect of "actual" rate on an electrode with LAMs, especially for cells that have low rate capability (as in the HE designs). It should be noted that, in conventional test regimes, the rate is calculated from the rated capacity of the cell and imposed at the cell level. It is often not attended at the electrode level (as the "actual" rate on the electrodes). This disparity in the rate could lead
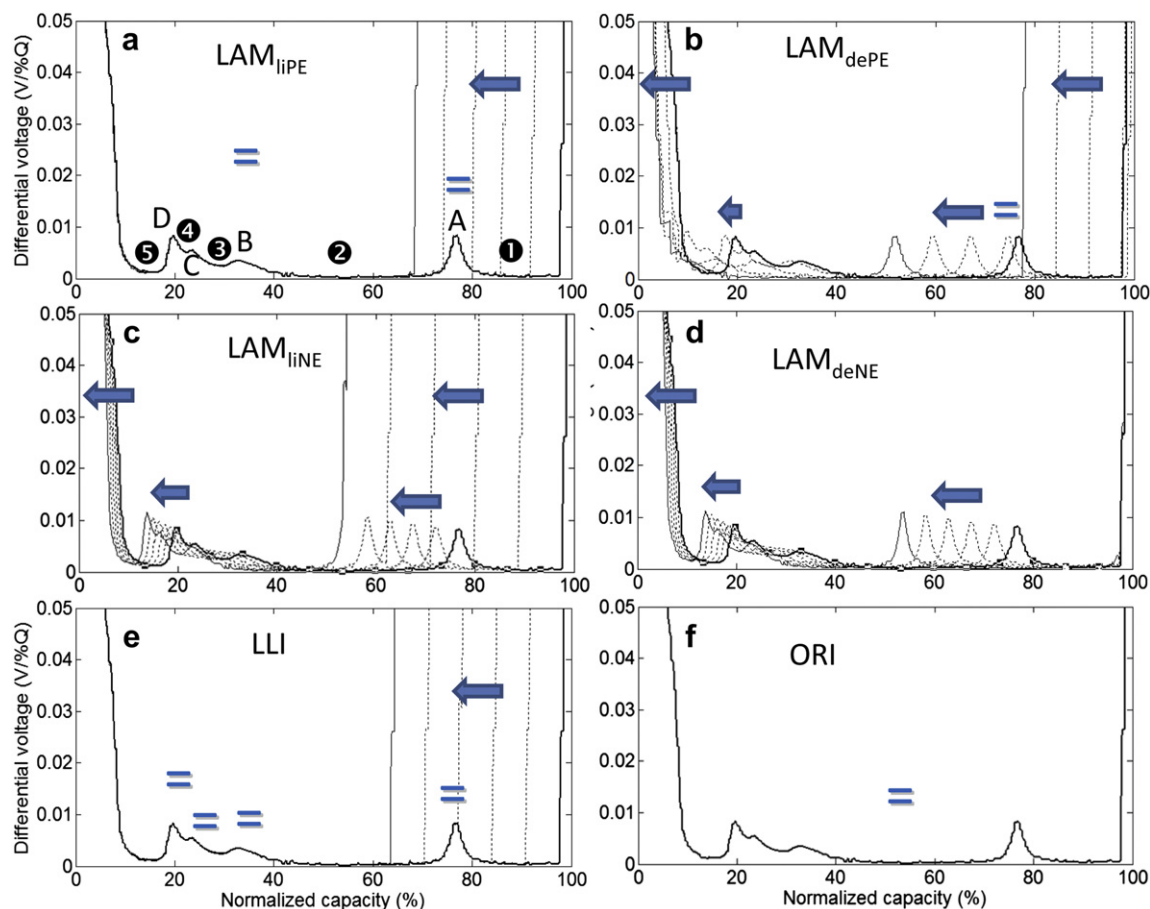
Fig. 14. DV signatures from the initial state (thick solid line) and at the end of 30% degradation (thin solid line) with 1/5th increment (dotted lines) for (a–d) each of the four LAMs, (e) LLI, and (f) a 100% ohmic resistance increase (ORI) at C/25.

to significant impacts on the electrode performance, while it might be less noticeable at the cell level. Fig. 16 presents an example where the evolution of the IC signatures with 30% LAM$_{liPE}$ are simulated. In the figure, the heavy solid line represents the initial state, the thin one the final state, and the dotted ones results in 6% increments. It is clear that the IC peaks are slowly shifting toward lower voltages. This would be interpreted as a polarization resistance increase, if a real cell were tested, whereas no ORI or FRD were included in the simulation. The shift of the IC peaks is in fact related to the increase of the "actual" rate on the PE that goes from about 2C to 3C (considering the same "imposed" rate on the cell, whereas only 2/3 of the active material on the PE are reacting to the current). Indeed, as shown in Fig. 5, when the "imposed" rate on the cell is increased, the IR drop shall cause the IC peaks shift toward lower voltages. This observation implies that the polarization resistance increase often reported in the literature upon degradation may not be entirely due to SEI layer growth or degradation in charge-transfer kinetics; to the contrary, some may be imputable to LAM that changed the "actual" rate at the electrode that is induced by degradation.

Interestingly, the same phenomenon could be interpreted for kinetic degradation as often observed in aging [6,30,36], since the EOD SOC is also increased if the rate is increased (Fig. 5). Moreover, LLI could also be responsible for an increase of EOD SOC toward the end of life (Fig. 11(b)). In this case, the RCV$_{EOD}$ should be stable, since the SOC evolution is caused by the reduction of the maximum capacity in the cell, not a change in kinetic performance.

Further investigations are in progress to de-convolute the effect of LAM on the FRD and ORI using some test data from commercial cell aging experiments.

5.3. Second stage of cell degradation

In the testing of commercial cells, it is often noticed that the capacity fade is rather constant in the first stage with a degradation mode associated with LLI. An accelerated capacity fade is observed in the second stage of degradation; typically, above 500 cycles [4,6] in today's cell designs. The second stage is often assumed to come from kinetic degradation accompanied with LAM [4,6,17,30,36]. The hypothesis mentioned in Section 5.2 could explain the co-appearance of the LAM and kinetic changes, but it could not explain why they appear so suddenly.

Figs. 6 and 7 provide some explanations for the sudden appearance of the second stage degradation. Some of the LAMs may be masked for up to 30% of capacity fade, if they occur on the electrode that is not capacity limiting to the cell performance. However, such degradation will eventually catch up with that of the limiting electrode and shift the roles in the capacity limiting mechanism over aging; thus, these LAMs finally become noticeable. Worse than that, since the LAM might be significant in magnitude already, its impact on the cell performance could appear more severely, as in an accelerated manner. Our model simulation suggests that a degradation mode may start benign but progress in a more aggressive manner in the aging; thus, it becomes prominent after certain incubation. This might be the
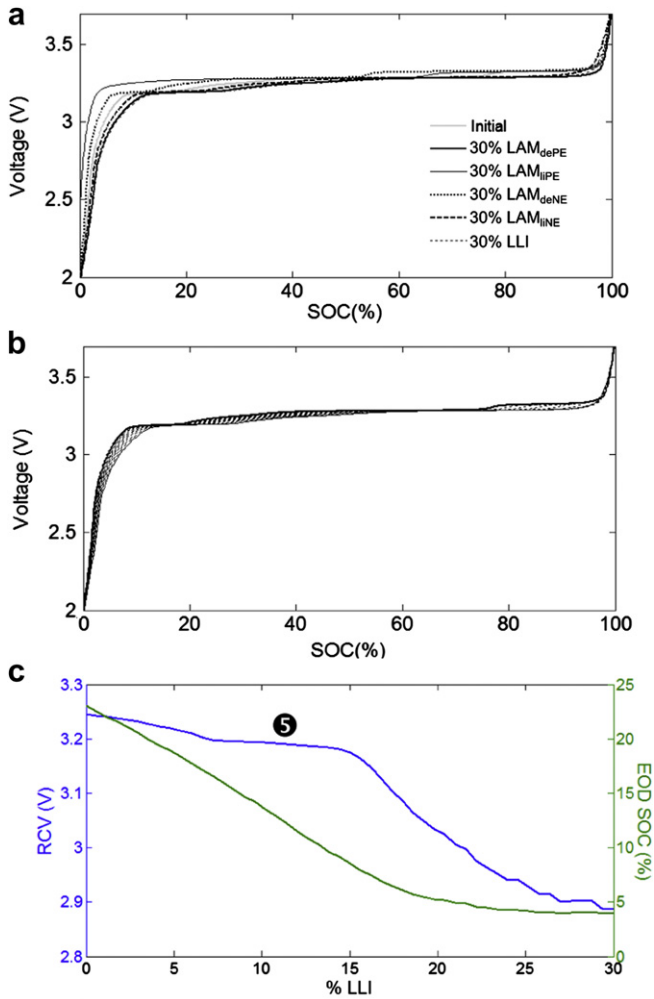
Fig. 15. Evolution of the ps-OCV = f(SOC) curve for (a) 30% capacity fade from each of the four types of LAM and LLI, (b) 30% LLI with 3% increments, and (c) associated evolution in RCV and EOD SOC as a function of %LLI.

case for the LAM$_{dePE}$ that incubates for a while, when LLI is occurring in a cell. Since LLI shifts the NE-to-PE loading correspondence in the same direction as LAM$_{dePE}$ (as shown in Figs. 6 and 7), the impact on capacity fade from LAM$_{dePE}$ might be
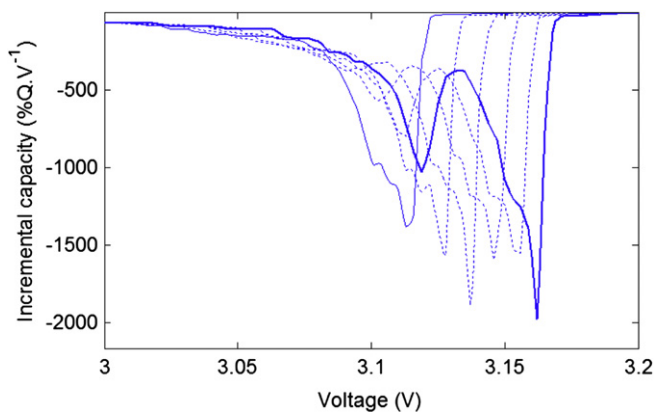

Fig. 16. IC signatures simulated with 30% LAM$_{liPE}$ for the HE design with 2C aging. The heavy solid line represents the initial state, the thin one the final state, and the dotted ones results in 6% increments.
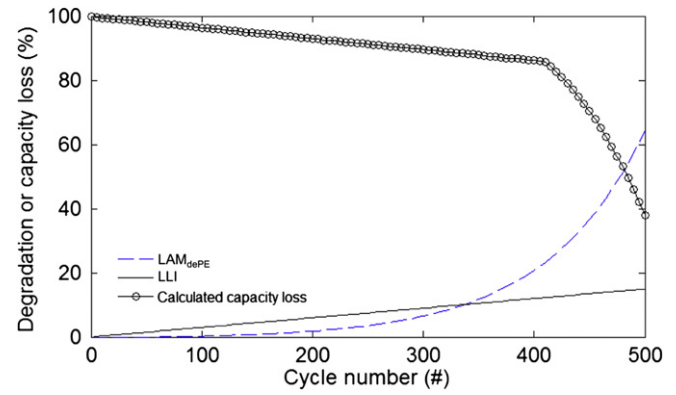

Fig. 17. Evolution of the capacity fade in a cell with linear LLI and exponential loss of LAM$_{dePE}$.

masked until it becomes prominent. Our experience suggests that LLI impacts capacity fade rather linearly in aging, whereas LAM may follow a power-law or exponential dependence [8]. This scenario is simulated in Fig. 17 where a linear 0.03%/cycle LLI is accompanied by an exponential LAM$_{dePE}$. After 400 cycles, the capacity fade is still driven primarily by LLI despite > 25% LAM$_{dePE}$. After 500 cycles, the LAM$_{dePE}$ starts to dominate the capacity fade at a higher pace. This capacity fade scenario is similar to the aging behavior of commercial cells observed in the laboratory tests [4,6].

6. Conclusion

For practical applications, one should realize that only a few parameters (likely time-resolved voltage, current, and temperature) might be available from the cell monitoring in the battery management systems (BMS), considering all costs, logistics, and scheduling issues in on-board, in-line battery diagnosis and prognosis. Therefore, any invasive characterizations or uses of complicated instrumentation are unrealistic and cost-prohibitive. It is essential to design simple diagnostic/prognostic tools and approaches for on-board, in-line battery monitoring and control that do not require costly, complicated monitoring/sensoring devices and computation overhead. To understand degradation modes in commercial cells over aging, a unique simulation capability is demonstrated here. This modeling approach is built from individual electrode behavior, including degradation modes, and proper adjustment of the loading ratio between the two electrodes in a cell design to achieve high fidelity in the simulation. This simulation capability offers great values to allow battery diagnosis and prognosis in BMS. The advantages of this approach are:

- A unique inference technique for battery diagnosis and prognosis,
- A mechanistic model that can synthesize a variety of cell aging scenarios based on degradation modes, including loss of active material, loss of lithium inventory, kinetic degradation or increase of polarization resistance, formation of parasitic phases, Li plating, and any combination of them,
- A physicochemical process-based model that constitutes from electrode-specific degradation modes to construct cell performance and degradation scenarios with consideration of cell designs and operating conditions,
- A versatile modeling tool without constraints on chemistry variations, cell designs, battery sizes and geometries, and operating or aging conditions.

Because of this capability, we illustrated some interesting degradation modes that were difficult to distinguish in the experiments but can be easily deciphered in this approach. For instance, loss of active materials could occur without detectable signatures in the beginning of aging but surface after an incubation period, as observed in some experiments with commercial cells.

Acknowledgments

References

[1] M. Dubarry, V. Svoboda, R. Hwu, B.Y. Liaw, Electrochem. Solid-State Lett. 9 (2006) A454–A457.
[2] M. Dubarry, V. Svoboda, R. Hwu, B.Y. Liaw, J. Power Sources 174 (2007) 366–372.
[3] M. Dubarry, V. Svoboda, R. Hwu, B.Y. Liaw, J. Power Sources 165 (2007) 566–572.
[4] M. Dubarry, B.Y. Liaw, J. Power Sources 194 (2009) 541–549.
[5] M. Dubarry, C. Truchot, M. Cugnet, B.Y. Liaw, K. Gering, S. Sazhin, D. Jamison, C. Michelbacher, J. Power Sources 196 (2011) 10328–10335.
[6] M. Dubarry, C. Truchot, B.Y. Liaw, K. Gering, S. Sazhin, D. Jamison, C. Michelbacher, J. Power Sources 196 (2011) 10336–10343.
[7] K. Honkura, H. Honbo, Y. Koishikawa, T. Horiba, ECS Trans. 13 (2008) 61–73.
[8] K. Honkura, K. Takahashi, T. Horiba, J. Power Sources 196 (2011) 10141–10147.
[9] I. Bloom, J. Christophersen, K. Gering, J. Power Sources 139 (2005) 304–313.
[10] I. Bloom, J.P. Christophersen, D.P. Abraham, K.L. Gering, J. Power Sources 157 (2006) 537–542.
[11] I. Bloom, A.N. Jansen, D.P. Abraham, J. Knuth, S.A. Jones, V.S. Battaglia, G.L. Henriksen, J. Power Sources 139 (2005) 295–303.
[12] I. Bloom, L.K. Walker, J.K. Basco, D.P. Abraham, J.P. Christophersen, C.D. Ho, J. Power Sources 195 (2010) 877–882.
[13] J. Christensen, J. Newman, J. Electrochem. Soc. 150 (2003) A1416.
[14] J. Christensen, J. Newman, J. Electrochem. Soc. 152 (2005) A818.
[15] Q. Zhang, R.E. White, J. Power Sources 179 (2008) 785–792.
[16] Q. Zhang, R.E. White, J. Power Sources 179 (2008) 793–798.
[17] M. Safari, C. Delacourt, J. Electrochem. Soc. 158 (2011) A1123.
[18] M. Safari, C. Delacourt, J. Electrochem. Soc. 158 (2011) A63.
[19] A.J. Smith, J.C. Burns, J.R. Dahn, Electrochem. Solid-State Lett. 14 (2011) A39.
[20] P. Liu, J. Wang, J. Hicks-Garner, E. Sherman, S. Soukiazian, M. Verbrugge, H. Tataria, J. Musser, P. Finamore, J. Electrochem. Soc. 157 (2010) A499.
[21] K. Kumaresan, Q. Guo, P. Ramadass, R.E. White, J. Power Sources 158 (2006) 679–688.
[22] M. Dubarry, B.Y. Liaw, J. Power Sources 174 (2007) 856–860.
[23] M. Dubarry, N. Vuillaume, B.Y. Liaw, J. Power Sources 186 (2009) 500–507.
[24] B.Y. Liaw, R.G. Jungst, G. Nagasubramanian, H.L. Case, D.H. Doughty, J. Power Sources 140 (2005) 157–161.
[25] B.Y. Liaw, G. Nagasubramanian, R.G. Jungst, D.H. Doughty, Solid State Ionics 175 (2004) 835–839.
[26] B.Y. Liaw, E.P. Roth, R.G. Jungst, G. Nagasubramanian, H.L. Case, D.H. Doughty, J. Power Sources 119–121 (2003) 874–886.
[27] M. Dubarry, C. Truchot, B.Y. Liaw, J. Power Sources (in preparation).
[28] W. Xing, J.R. Dahn, J. Electrochem. Soc. 144 (1997) 1195–1201.
[29] J. Shim, K.A. Striebel, J. Power Sources 119–121 (2003) 955–958.
[30] P. Ramadass, B. Haran, R. White, B.N. Popov, J. Power Sources 112 (2002) 614–620.
[31] B.V. Ratnakumar, M.C. Smart, ECS Trans. 25 (2010) 241–252.
[32] M. Kerlau, M. Marcinek, V. Srinivasan, R. Kostecki, Electrochim. Acta 52 (2007) 5422–5429.
[33] Y. Xia, Y. Zhou, M. Yoshio, J. Electrochem. Soc. 144 (1997) 2593–2600.
[34] H. Zheng, Q. Sun, G. Liu, X. Song, V.S. Battaglia, J. Power Sources 207 (2012) 134–140.
[35] N. Sharma, V.K. Peterson, M.M. Elcombe, M. Avdeev, A.J. Studer, N. Blagojevic, R. Yusoff, N. Kamarulzaman, J. Power Sources 195 (2010) 8258–8266.
[36] P. Ramadass, B. Haran, R. White, B.N. Popov, J. Power Sources 123 (2003) 230–240.
[37] J.-F. Martin, M. Cuisinier, N. Dupré, A. Yamada, R. Kanno, D. Guyomard, J. Power Sources 196 (2011) 2155–2163.
[38] M. Cuisinier, J.-F. Martin, N. Dupré, R. Kanno, D. Guyomard, J. Mater. Chem. 21 (2011) 18575.
[39] N. Marx, L. Croguennec, D. Carlier, L. Bourgeois, P. Kubiak, F.d.r.L. Cras, C. Delmas, Chem. Mater. 22 (2010) 1854–1861.
[40] K. Zaghib, C.M. Julien, J. Power Sources 142 (2005) 279–284.
[41] C. Masquelier, P. Reale, C. Wurm, M. Morcrette, L.c. Dupont, D. Larcher, J. Electrochem. Soc. 149 (2002) A1037.
[42] W. Lu, C.M. Loópez, N. Liu, J.T. Vaughey, A. Jansen, D.W. Dees, J. Electrochem. Soc. 159 (2012) A566.
[43] M. Dubarry, V. Svoboda, R. Hwu, B.Y. Liaw, J. Power Sources 174 (2007) 1121–1125.